#### **Abstract**

Synthesis of Naphthalimide Derivative and Diketopyrrolopyrrole (DPP)-Based [2]Rotaxane/Polyrotaxane as Novel Chemosensor Materials and a Controllable Hierarchical Nano Self-Assembled Structure from Polyrotaxane

Student: M. V. P. S. K. R. Raju Advisor: Hong-Cheu, Lin

The pivotal objective of this dissertation is to construct novel orthogonally H-bonded mechanically interlocked molecular/polyrotaxane architectures with an asymmetric (Diketopyrrolopyrrole) stopper and to study their molecular shuttling process under solvent, anion, and acid-base stimuli control along with their controllable hierarchical nanostructure formations plugged with positive cooperativity non-covalent interactions. In the introduction of this doctoral thesis we have introduced brief early synthetic attempts to create mechanically interlocked molecules (MIMs) such as rotaxanes and catenanes as well as their polymeric counterparts. Moreover novel templating methodologies to build MIMs and some latest examples of MIMs based molecular shuttles under various stimuli control were also introduced. Fundamentally, underplayed chemo sensing mechanisms in these systems were presented. Meanwhile, we have developed a novel and facile fluorescent ratiometric chemodosimeter for grisly toxic hydrazine via mild Ing-Manske phthalimide deprotection method in this doctoral thesis as well.

In chapter two, a novel [2]rotaxane based on an orthogonal H-bonded motif and 3,6-di(thiophen-yl)pyrrolo[3,4-c]pyrrole-1,4(2H,5H)-dione (**DPP**) with controlled topicity was successfully constructed, displaying excellent stimulated responses toward anion and solvent polarity. The extensive <sup>1</sup>H & <sup>19</sup>F NMR titrations were lucidly revealed the binding site and the mode binding interaction as well. The preorganized host selectively recognized F with high optical sensitivity and reversibility via enhanced positive cooperativity and noncovalent interaction by evidence of a shorter fluorescence lifetime. Therefore we developed a first prototype [2]rotaxane molecular shuttle for selective recognition of F with high optical outputs.

In chapter three, four analogous polymers were systematically synthesized by copolymerization of 9-alkylidene-9*H*-fluorene monomer with various monomers, which diketopyrrolopyrrole unit tethered with a dumbbell unit, a metalated [2]rotaxane, a demetalated orthogonal H-bonded [2]rotaxane, and a simple alkyl chain, to furnish P1, P2, P3, and P4, respectively, to investigate the supramolecular interactions of the mechanically interlocked rotaxane pendants and conjugated polymer backbones. Prevailing <sup>1</sup>H NMR and UV-vis to NIR titration profiles indicated that the novel polyrotaxane P3 showed a sensitive and reversible acid-base molecular switch capability via supramolecular interactions in contrast to the other polymers (P1, P2, and P3). Compared with the other polymers, P3 possessed a narrower bandgap, which was also confirmed by the computational study. Prominently, the monitoring of a controllable nano-selfassembly process of P3 was obtained by reversible acid-base molecular switch approaches. The orthogonal H-bonded pendant [2]rotaxane unit and the steric demand of P3 judiciously allowed to morph into a hierarchical nanostructure via interconvertible H-bonds, anion- $\pi$  and  $\pi$ - $\pi$  stackings, as well as hydrophobic interactions.

In chapter four, A facile and sensitive fluorescent probe for hydrazine based on phthalimide appended hydrophilic naphthalimide was successfully constructed, displaying excellent colorimetric and ratiometric responses towards hydrazine via Ing-Manske phthalimide deprotection conditions in semi-aqueous buffer solution. The estimated detection limit was as low as 4.2 nM (hydrazine content = 1 ppb) far below than the threshhold limit value (TLV) of 10 ppb according to the U. S. Environmental Protection Agency (EPA). Prevailing detection of hydrazine in living cells of the current probe is demonstrated.

Thus in conclusion, a novel archetype **DPP** based highly fluorescent [2]rotaxane was developed. The remarkable stimulated responses towards solvent polarity and fluoride ion were discussed. Moreover, the extended efforts of this current design into polyrotaxane architectures along with their acid-base controllable hierarchical nanostructure formations via reversible optical molecular switch approaches coupled with various non-covalent interactions were discussed. Furthermore a novel fluorescent ratiometric chemodosimeter for hydrazine based on Ing-Manske phthalimide deprotection was presented in detail.

#### **Chinese Abstract**

合成 Naphthalimide 衍生物與含 Diketopyrrolopyrrole (DPP)為基底之[2]Rotaxane/Polyrotaxane作為新穎化學感測材料及可操控規則奈米自組裝結構之Polyrotaxane

Student: 馬瑞奇 Advisor: 林宏洲 教授

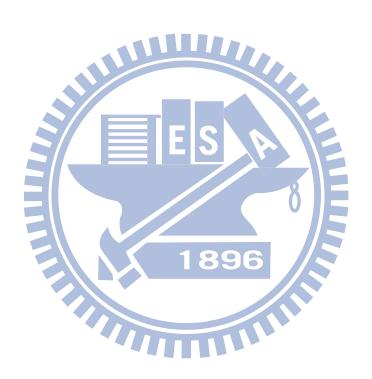
本論文的主要目標是合成新的正交氫鍵機械互鎖/聚輪烷分子不對稱結構(二酮吡咯並吡咯)塞,並研究其在溶劑條件、陰離子及酸鹼刺激下控制分子的穿梭過程並調控其納米結構的形成插入正協同非共價相互作用。在本博士論文中,我們已經簡短介紹了的早期嘗試合成如輪烷和索烴及其聚合物機械互鎖分子(MIMS)。此外,我們介紹了新穎的模板方法合成MIMS和一些最新的例子基於 MIM 的分子梭在各種環境刺激下控制。從根本上來說,在這些系統裡化學感測正在被運用。同時,在這個博士論文中我們已開發出一種新型和淺顯的螢光比例來測定有毒肼並透過緩和的 Ing-Manske 鄰苯二甲酰亞胺去保護的方法。

在第二章中,成功建構一種新型的[2]輪烷的基礎上正交氫鍵和 3,6 - 二(噻吩基)吡咯並 [3,4-C]吡咯-1,4(2H,5H) - 二酮(**DPP**)與控制 topicity,表現出對陰離子和溶劑極性優異的 刺激反應。廣泛的運用 <sup>1</sup>H 和 <sup>19</sup>F NMR 滴定顯示出的結合位點和模式以及結合相互作用。其中證明了 preorganized 會選擇性地確認 F-光靈敏度高和可逆性通過增強的正協同和非共價相 互作用的螢光壽命較短。因此,我們開發出了新型的選擇性氣離子光學[2]輪烷的分子開關。

在第三章中,四個類似的系統合成聚合物共聚單體與各種單體,含有二酮吡咯並吡咯單元與啞鈴單元拴,金屬化[2]輪烷,demetalated 的正交氫鍵 9 亞-9H-芴[2]輪烷,和一個簡單的烷基鏈,透過 P1, P2, P3 和 P4, 分別研究的機械聯鎖的輪烷的垂飾和共軛聚合物骨架的超分子相互作用機制。運用 <sup>1</sup>H NMR 和紫外可見近紅外滴定的檔案證明了新型聚輪烷 DMRTP 通過對比其他聚合物 (P1, P2 和 P3) 本身是一個敏感的且在酸鹼溶液下分子開關能力為可逆的超分子相互作用。 P3 與其他聚合物相比,具有更窄的帶隙,這也經過計算研究證實了。特別的是,一個可控的納米自組裝過程 P3 的監測可藉由可逆酸鹼分子開關的方法來驗證。正交氫鍵垂飾[2]輪烷單元可以變形到一個納米次結構並藉由相互轉換的 H-bond,陰離子-π 和 π-πstackings,以及疏水性相互作用。

在第四章,成功的合成肼苯二甲酰亞胺附加親水 naphthalimide,顯示出優異的色度和比例 對肼的反應,通過 Ing-Manske 鄰苯二甲酰亞胺半水緩衝溶液中去保護條件是一種簡便和敏感 的螢光探測。估計檢測限低至 4.2 nM ( H 含量= 1 ppb ) 根據美國環境保護署 (EPA) ,遠遠低於閾值限值 (TLV) 為 10 ppb 。證明肼電流對於活細胞檢測的可行性。

因此,一種新型的基於 archetype **DPP** 高螢光[2]輪烷的開發。討論了溶劑極性和氟離子的刺激的反應。此外,該電流的設計隨著酸鹼調控的層次加上透過可逆的光學分子開關的方法,以及各種非共價相互作用的納米結構形成的聚輪烷的體系結構擴展進行了多方討論。此外,對於 Ing-Manske 鄰苯二甲酰亞胺脫肼一種新型的螢光比例 chemodosimeter 做了詳細介紹。



#### Acknowledgements

First and foremost I would like to thank my advisor Prof. Hong-Cheu Lin, for giving me the opportunity to carry out research described in this doctoral thesis. I deeply appreciate all his contributions of time, patience, motivation, immense knowledge ideas, and funding to make my Ph.D. experience productive and stimulating.

I would like to thank Professor Chen, San-Yuan (Chairman), and all other professors and secretaries of Department of Materials Science and Engineering, NCTU. The financial support of my Ph.D. work granted by National Science Council (NSC), Office of International Affairs and NCTU are greatly acknowledged. I owe my special thanks to 2D-NMR, MALDI mass and other analysis team members of NCTU for their inevitable timely and precious help.

I owe my deepest gratitude to Prof. Satyannarayana and Prof. R. Venkateswarulu for their immense and instrumental early support during my Master studies as well as their motivational teaching and research styles which driven me towards the chemistry as my future career. I wish to thank all my current and previous lab mates for their co-operation in my research. I would also like to thank myriads of my friends in various institutes, of Taiwan and back home (India) for their timely, valuable, and constructive help in key areas.

Last but not least, my greatest gratitude to my father for his eternal blessings. Immeasurable deepest gratitude to my mother for her sacrifices to provide me a better education and a rising career, she transported to me a vital patience as my first teacher. Finally, I am extremely thankful to my beloved brother Anil for his early and matured support to my family and my education as well.

## **Table of Contents**

Abstract		I
Chinese abs	tract	III
Acknowledg	gments	V
Table of Cor	ntents	VI
List of Schen	mes	X
	es	
List of Figu	res	XII
Chapter 1.	Introduction	1
1. 1 Sup	ramolecular chemistry.	1
1.1.1	Pseudorotaxanes, Rotaxanes, Catenanes, and Borromean rings	2
1.1.2	Polyrotaxane architectures	4
1.1.3	Early synthetic attempts to construct MIMS.	
1.1.4	Principles to build MIMs and MIPAS 9.6.	8
1.1.5	Modern supramolecular templating methodologies to create MIMs	10
1.1.6	Fluorescent chemosensing applications of via molecular shuttle	
	approach under external stimuli	15
1. 2 Che	emosensors: Principles and mechanisms.	24
1.2.1	Classification of chemosensors.	25
1.2.2	Intramolecular charge transfer (ICT)	26
1.2.3	Photo induced electron transfer (PET)	27
1.2.4	Photo induced charge transfer (PCT)	29
1.2.5	Electronic energy transfer (EET).	30

1.2.6 Fluorescence resonance energy transfer (FRET)	32
1.2.7 Ratiometric chemodosimeters.	
1. 3 Literature survey.	36
1.3.1 Solvent and Anion controllable [2]rotaxane molecular shuttles	36
1.3.1.1 Solvent driven molecular shuttles	36
1.31.2 Anion driven molecular shuttles.	37
1.3.2 Polyrotaxane Shuttles and their Controllable Self-assembly to form	
Hierarchical Nanostructures.	
1.3.2.1 Polyrotaxane shuttles	41
1.3.2.2 Controllable molecular self-assembly of polyrotaxanes and their	
Nanostructures	43
1.3.3 Fluorescent Chemosensors for Hydrazine.	46
1. 4 Research Motive	49-50
Chapter 2. A Novel Diketopyrrolopyrrole (DPP)-Based [2]rotaxane for Highly	Selective
Optical sensing of Fluoride	
2. 1 Introduction	51
2. 1 Introduction	53
2.2.1 General methods and materials	53
2.2.2 Stock solution preparation	55
2.2.3 Synthesis of compound 1, compound 2, and DPP derivative 3	55
2.2.4 Synthesis of compound 1-C, [2]Rotaxane 2-M, and [2]Rotaxane 2-P	57
2.2.5 Synthetic procedures.	58
2. 3 Results and Discussion.	70
2.3.1 <sup>1</sup> H NMR titrations studies.	70
2.3.2 <sup>19</sup> F NMR titrations studies	75

2.3.3 UV-vis & Fluorescence titrations studies	76
2.3.4 Electrochemical titrations.	81
2.3.5 Time resolved photo luminescence studies	82
2. 4 Conclusions	83
Chapter 3. An Acid-Base Controllable Hierarchical Nano structure from a NIR-Al	bsorbing
Conjugated Polyrotaxane-Based Optical Molecular Switch	84
3. 1 Introduction	84
3. 2 Experimental section.	87
3.2.1 General methods and materials.	87
3.2.1 General methods and materials	89
3.2.3 Calculation methods	89
3.2.3 Calculation methods	90
3.2.5 Synthesis of AKF donor, DPP derivative, and rotaxanated copolymers	90
3.2.6 Synthetic Procedures	93
3.2.7 General Polymerization method & Polymers data	95
3. 3 Results and Discussion.	98
3.3.1 Gel Permeation Chromatography (GPC) and 2D-DOSY NMR	
Characterization of MIPA.	98
3.3.2 <sup>1</sup> H NMR Spectroscopic Studies.	99
3.3.3 Optical and Electrochemical Measurements	105
3.3.4 Theoretical Calculations	112
3.3.5 Microscopic and DLS of Controllable Hierarchical	
Nano-self-Assemblies of MIPAs	121
2. A Conclusions	121 122

Chapter 4. A Facile Ratiometric Fluorescent chemodosimeter for hydra Applications in living cells	
4. 1 Introduction.	133
4. 2 Experimental section.	135
4.2.1 General methods and materials	135
4.2.2 Stock solutions	136
4.2.3 Design strategy	136
4.2.4 Synthetic Procedures.	137
4. 3 Results and Discussion	139
4.3.1 UV-vis and Fluorescence-based sensing studies of probe <b>HZ</b>	
4.3.2 Studies to realize ratiometric signalling mechanism of probe <b>HZ</b>	144
4.3.3 Time effects on ratiometric signalling.	
4.3.4 Screening the selectivity of probe <b>HZ</b>	149
4.3.5 pH effects on ratiometric signalling of probe <b>HZ</b>	151
4.3.6 Confocal imaging of probe <b>HZ</b> in living cells	
4. 4 Conclusions	155
Chapter 5. Conclusions	157
References.	
Author Information & Publications.	174

#### **List of Schemes**

## **List of Tables**

Table 3. 1 UV-vis to NIR absorption and electrochemical data of monomer 2-b and p	polymers P1,P2
P3, and P4, respectively	111
Table 3. 2 TD-DFT calculated HOMO, LUMO, HOMO-LUMO gap (HLG), wavelet	ngth $(\lambda_{max})$ , and
oscillator strength (f) for D1 D2 and A1	119



# **List of Figures**

Figure	1.1	Cartoon	representation	on of (a)	[2]catena	ne, (b)	[2]rotaxan	e, and	(c)	Borromean
rings										3
Figure 1	.2 S	ynthesis o	of [2]rotaxane	and [2]cat	enane via t	the forma	ation vital p	seudoro	taxaı	ne
precurso	r								•••••	3
Figure		1.3	Cartoon	represer	ntations	of	some	of		main-chain
polyrotax	kane	S								5
Figure 1	. <b>4</b> C	artoon re	presentation o	f some of	side-chain	polyrota	xanes			5
Figure 1	<b>.5</b> S	chill's ch	emical conver	sion rotax	ane synthes	sis				7
_		_	s's passive c					_		
[2]catena	ine						E			7
Figure 1	. <b>7</b> T	he solid	state structure							
derivativ	es				100					8
			orinciples of ro	otaxane ass	sembly		••••			9
Figure 1	.9 P	rinciple a	pproaches of p	oolyrotaxa	ne assembl	y				9
Figure 1	.10	Synthesis	of the first an	nide linked	[2]rotaxar	nes accor	ding to Vo	gtle et. a	1	10
Figure 1	.11	The synt	hesis and med	chanism of	f peptidoro	taxanes	by five mo	olecules	H-bo	ond directed
assembly								• • • • • • • • • • • • • • • • • • • •		11
Figure 1	.12	Stoddart	[2]rotaxane ba	ased on py	ridine crov	wn ether	and secon	dary am	mon	ium salt via
H-bondir	ıg									12
Figure 1	.13	Synthesis	of [2]rotaxan	e via Beer'	's interwea	ving anio	on templati	on strate	<b>2</b> V	13

Figure 1.14 Schematic illustration of the principles of active metal template synthesis. The formation
of a covalent bond between the orange and green "half-thread" units to generate the rotaxane thread
is promoted by a metal catalyst (shown in grey) by the metal ion coordination requirements. (a)
Stoichiometric active metal template synthesis of a [2]rotaxane: (i) template assembly and covalent
bond forming catalysis; (ii) subsequent demetallation. (b) Catalytic active metal synthesis of a
[2]rotaxane (only a sub-stoichiometric amount of the is required as it turnover during
reaction
<b>Figure 1.15</b> Cartoon representation of molecular shuttle
Figure 1.16 Light driven naphthalimide [2]rotaxane molecular shuttle with dual fluorescence
addresses
Figure 1.17 Pyrene and perylene stoppered [2]rotaxane molecular shuttle under pronated cis-trans
isomerization with energy transfer characteristics
Figure 1.18 Synthesis of perylene [2]rotaxane via Vogtle template method.
Figure 1.19 Chemical structure and UV-vis spectra of squaraine derived [2]rotaxane
Figure 1.20 Chemical structure and intracellular bio imaging of fluoresceinated peptides under
[2]rotaxane host
<b>Figure 1.21</b> PET process in a cyclodextrin-oligothiophene based 2T-[2] rotaxanes21
Figure 1.22 Acid-base controllable NDI based [2]rotaxane molecular shuttle via ICT21
Figure 1.23 Donor-acceptor based [2]rotaxane molecular shuttle via PCT and emission exciplex
process
Figure 1.24 FRET process across mechanical bond of a [2]rotaxane.
Figure 1.25 Electron transfer process between ferrocenated wheel and fullerene stoppered H-bond
templated [2]rotaxane

<b>Figure 1.26</b> Principal stages in the operation of a sensor.
Figure 1.27 Classification of chemosensors.
Figure 1.28 Solvent effect on absorption spectral wavelength for a fluorophore with an ICT excited
state. FC represents a Franck-Condon excited state. "Equil." represents a thermally equilibrated
electronic ground state. The dipole of the ground state is assumed to be small. $S_0$ and $S_1$ represent the
electronic ground and lowest energy excited states, respectively
Figure 1.29 Solvent effect on emission spectral wavelength for a fluorophore with an ICT excited
state. "Thexi" represents a thermally equilibrated electronic excited state The other terms are defined
under <b>Figure 1. 28</b>
Figure 1.30 Principle of analyte detection by fluorescent PET sensors
Figure 1.31 Spectral displacements of PCT sensors resulting from interaction of a bound cation with
an electron-donating or electron-withdrawing group
<b>Figure 1.32</b> Lindsey's porphyrin arrays for productive EET into an energy.
Figure 1.33 A spectral overlap (marked in diagonal lines) between the donor emission and the
Acceptor absorption is required for fluorescence resonance energy transfer (FRET) between donor
and acceptor fluorophores.
<b>Figure 1.34</b> Two principle working modes of a fluorescent chemodosimeter
<b>Figure 1.35</b> A NDI and ICT based ratiometric Chemodosimeter for H <sub>2</sub> O <sub>2</sub> 35
<b>Figure 1.36</b> Multistationed peptide-based molecular shuttles under solvent polarity
Figure 1.37 Solvent driven copillar[5] arene based molecular spring

Figure 1.38 Electronic/energy transfer between ferrocenated macrocycle and pyrene stopper
[2]rotaxane with high contrast fluorescent molecular shuttle under solvent control.
37
Figure 1.39 Anion formation induced macrocycle translocation in Leigh peptide-based molecular
shuttle
<b>Figure 1.40</b> Cl <sup>-</sup> binding induced macrocycle translocation in squaraine based [2] rotaxane38
<b>Figure 1.41</b> Cl <sup>-</sup> binding of a ruthenium complex appended [2]rotaxane molecular shuttle39
<b>Figure 1.42</b> SO <sub>4</sub> <sup>2-</sup> binding of a naphthalene congaing [3]rotaxane molecular shuttle39
<b>Figure 1.43</b> TBAF triggered two-stage retractable functions of [2]rotaxane shuttle
Figure 1.44 TBAF driven reversible contracted and stretched forms of [2]rotaxane
Figure 1.45 TBAF and acid/base driven reversible morpholin-naphthalimide [2]rotaxane molecular
Figure 1.46 Rotaxanated conjugated sensory polymer for acidic alcoholic vapors.
41
Figure 1.47 Polyplex formation of DMAE-SS-PRX and its pDNA release by supramolecular
dissociation
<b>Figure 1.48</b> Changes in fluorescence induced by host-guest complexes in a CD polyrotaxane42
<b>Figure 1.49</b> A supramolecular cross-linked network as a multiple fluorescent sensor
Figure 1.50 SEM image presenting a 3D-hexagonal microfiber as drawn from a $\alpha$ -CD and PEG
inclusion complex
Figure 1.51 Immobilized self-assembly of CP and aligner under RCM condition. TEM images
denoting CP-aligner self-assembled structures before and after TFA treatment.

Figure 1.52 Donor/acceptor based poly[2]catenane and its drop casted SEM self-assemble images.
45
Figure 1.53 Single helical nanostructure drawn from a calix[4]arene-α-CD based supramolecular
chiral polyrotaxane
Figure 1.54 Coumarin levulinated fluorogenic and chromogenic probe for selective detection of
Hydrazine46
Figure 1.55 7-diethylamino-1,4-benzoxazine-2-one (DEAB) and ICT based ratiometric probe for
hydrazine
<b>Figure 1.56</b> Coumarin based chromogenic and ratiometric probe for Hydrazine
<b>Figure 1.57</b> Dichlorofluorescein and resorufin based dual signaling probe for Hydrazine
Figure 1.58 Conjugated polymethine $\pi$ -electron contained cyanine derivative (Cy7A) for selective
ratiometric sensing of hydrazine in NIR-region
Figure 2.1 Solvent polarity changes and anion tetrabutylammonium fluoride (TBAF) driven highly
contrasted fluorescent DPP based reversible [2]rotaxane molecular
shuttles
Figure 2.2 <sup>1</sup> H NMR spectra (CDCl <sub>3</sub> , 300 MHz, 298 K): (a) macrocycle, (b) 1:1 mixture of control
axle 1-C and macrocycle, (c) 1-C, (d) [2]rotaxane 2-P. The assignments correspond to the lettering
shown in Scheme 2. 2. (numerical and alphabetical lettering indicating dumbbell part and
macrocycle, respectively)
<b>Figure 2.3</b> <sup>1</sup> H NMR spectra (300 MHz, 298 K): (a) [2]rotaxane translational isomer <b>2-P</b> in CDCl <sub>3</sub> ,
(b) [2]rotaxane translational isomer <b>2-R</b> in $d_6$ -DMSO. The assignments correspond to the lettering
shown in <b>Scheme 2. 2</b> .

in DMSO); (b) fluorescence of translational isomer 2-P (in DCM) and translational isomer 2-R (in
DMSO). ( $\lambda_{ex} = 525 \text{ nm}$ )
Figure 2.11 (a), (b) UV-Vis and fluorescence spectral changes of 2-R (1 x 10 <sup>-5</sup> M in DMSO) upon
the addition of TBAF in DMSO (0-40 equiv), respectively. Inset pictures in (a) and (b) indicating
naked eye color changes as well as fluorescence changes under UV light (365 nm) upon the addition
of TBAF, respectively $(\lambda_{ex} = 525 \text{ nm})$
Figure 2.12 (a) Fluorescence spectral responses of 2-R were utilized in determining the
stoichiometry for 2-R/F complex, change in the fluorescence intensity multiplied by guest mole
fraction was plotted against guest mole fraction. Indicating 1:1 Binding stoichiometry for the 2-R/F
complex (total concentration 200 µM); (b) calculation of binding constant for <b>2-R</b> /F complex using
Connors method; (c) stern-volmer plot of I/Io ( $\lambda_{em} = 582 \text{ nm}$ ) vs [F]; (d) histograms representing the
fluorescence spectral changes of [2]rotaxane 2-R with the addition of 40 equiv of different anions.
78
Figure 2.13 UV-vis absorption and fluorescence spectral changes of 2-R, 2-M, and 1-C (all
receptors concn = $1 \times 10^{-5}$ M, DMSO) with the addition of 40 equiv of different anions as TBAX (X
= F <sup>-</sup> , Cl <sup>-</sup> , Br <sup>-</sup> , I <sup>-</sup> , AcO <sup>-</sup> , NO <sub>3</sub> <sup>-</sup> , and H <sub>2</sub> PO <sub>4</sub> <sup>-</sup> ); (a), (b) UV-Vis absorption and fluorescence spectral
changes of 2-R, respectively; (c), (d) UV-Vis absorption and fluorescence spectral changes of 2-M,
respectively; (e), (f) UV- absorption and fluorescence spectral changes of 1-C, respectively. (for all
the samples fluorescence was monitored at their respective emission maxima by exciting at 525
nm)
<b>Figure 2.14</b> (a) Naked eye color changes of [2]rotaxane <b>2-R</b> (1 x 10 <sup>-5</sup> M, DMSO) with the addition
of various anions (30 equiv in DMSO); (b) fluorescence changes of samples mentioned in (a) under
UV light (365 nm); (c) naked eye color changes of 2-R and its precursors 1-C and 2-M with the

addition of 30 equiv TBAF; (d) fluorescence changes of samples mentioned in (c); (e) as depicted in
the inset picture of 2-R fluorescence spectra , fluorescence changes of (A) 2-R free, (B) after
addition of TBAF to sample (A), and (C) is recovered sample with the addition of TFA to sample (B)
under UV light (365 nm); (f) fluorescence intensity changes of <b>2-R</b> (1 x 10 <sup>-5</sup> M, DMSO) at 582 nm
under addition of alternate compounds (TBAF and TFA) for four cycles ( $\lambda_{ex} = 525$ nm).
80
Figure 2.15 Electrochemical titration studies of 2-P (3 mM) using 0.1M TBAPF <sub>6</sub> supporting
electrolyte at a scan rate of 0.1Vs <sup>-1</sup> in CHCl <sub>3</sub> : a) changes in electrochemical potential of 2-P with
TBAF (30 mM) upon progressive addition from 0-10 equiv; b) plot of potential change in mV
against fluoride equiv81
Figure 2.16 Time resolved fluorescence spectral changes of [2]rotaxane 2-R before and after the
addition of TBAF82
Figure 2.17 Time resolved fluorescence spectral responses for 1-C and 2-M before and after
addition of TBAF
Figure 3.1 Acid-base driven reversible molecular shuttling process in a conjugated side-chain
polyrotaxane having an orthogonal topological cavity and its controllable hierarchical nanostructure
formation mechanism along with high contrast optical functions
Figure 3.2 Gel permeation chromatographs of polymers P4 and P3
<b>Figure 3.3</b> (a) <sup>1</sup> H NMR (600 MHz, CDCl <sub>3</sub> , 298 K) stock plot of monomer <b>2-b</b> and polymer <b>P3</b> and
(b) 2D-DOSY (600 MHz, CDCl <sub>3</sub> , 298 K) NMR spectra of P3 at a concentration of 12 mg/ml.
Diffusion coefficient of MIPA, axle part, and free monomer were marked with circles. The
assignments correspond to the lette shown in Scheme 1

Figure 3.4 2D-DOSY (600 MHz, CDCl <sub>3</sub> , 298 K) NMR spectra of P2 at a concentration
of 12 mg/ml. Diffusion coefficient of P2, axle part, and monomer were marked with
circles
Figure 3.5 Changes in <sup>1</sup> H NMR (300 MHz, CDCl <sub>3</sub> , 298 K) spectrum of [2]rotaxane 2-b (3 mM)
during titration with TFA (0-4 equiv). The assignments correspond to the lettering shown in Main
Scheme 1
<b>Figure 3.6</b> Job plot between monomer <b>2-b</b> and TFA obtained by plotting $\Delta\delta$ in chemical shift for <b>2-b</b>
pyridine proton (13) observed by <sup>1</sup> H NMR against the change in mole fraction of guest X <sub>guest</sub> 102
<b>Figure 3.7</b> <sup>1</sup> H NMR (CDCl <sub>3</sub> , 300 MHz): <b>2-b</b> (CDCl <sub>3</sub> , $c = 3$ mM); TFA (CDCl <sub>3</sub> , $c = 30$ mM): (a) free
monomer <b>2-b</b> . (b) <b>2-b</b> + TFA 1.0 eq. (c) TFA containing monomer <b>2-b</b> recovered with the addition
of DBU102
Figure 3.8 VT-NMR (500 MHz, CDCl <sub>3</sub> ) Stock plot of monomer 2-b in the presence of TFA; (a) 2-b
+ TFA (1.0 equiv), 233 K. (b) <b>2-b</b> + TFA (1.0 equiv), 298 K. (c) free <b>2-b</b> , 298 K. (d) <b>2-b</b> + TFA (1.0
equiv), 323 K. The assignments correspond to the lettering shown in Scheme 1
Figure 3.9 IR-chromatographs of monomer 2-b (marked black) and complex 2-b-TFA (marked red).
Inset picture is showing a noticeable new band for complex 2-b-TFA indicating strong H-bonded
interactions 104
Figure 3.10 UV-vis to NIR absorption spectra of polymers P1, P2, P3, and P4 (a) in chloroform
solution; (b) films on quartz plates
Figure 3.11 (a) and (b) UV-vis and fluorescence spectral changes of 2-b (10 $\mu$ M in DCM) upon the
addition of TFA in DCM (0 - 10 equiv), respectively. Insets: pictures in (a) and (b) indicate naked
eye color changes as well as fluorescence changes under UV light (365 nm) upon the addition of
TFA, respectively ( $\lambda_{\text{ex}} = 525 \text{ nm}$ )

Figure 3.12 (a) and (b) UV-vis and fluorescence spectral changes of P3 (10 $\mu$ M in THF) upon the
addition of TFA in THF (0 - 8 equiv), respectively. Insets: pictures in (a) and (b) indicate naked eye
color changes as well as fluorescence changes under UV light (365 nm) upon the addition of TFA,
respectively. ( $\lambda_{ex}$ =720 nm).
Figure 3.13 (a) and (b) calculation of binding constants for 2-b-TFA and P3-TFA using Connors
method, respectively; (b) and (d) fluorescence intensity changes of <b>2-b</b> and <b>P3</b> (10 $\mu$ M, DCM) at 580
and 766 nm under addition of alternate compounds (TFA and DBU) for 4 cycles with ( $\lambda_{ex} = 525$ and
720 nm), respectively. (e) and (f) fluorescence changes without acid (a), with acid (b), and recovered
fluorescence by addition of DBU (c) of 2-b and P3, respectively. Insets denoting their respective
fluorescence changes under UV light (365 nm)
Figure 3.14 (a) and (b) fluorescence changes of monomers 1-a and 2-a (10 $\mu$ M in DCM) without
acid and with the addition of (TFA, 30 equiv), respectively. (c) and (d) fluorescence changes of
polymers P1 and P2 (10 $\mu$ M in THF) without acid and with the addition of (TFA, 30 equiv),
respectively
Figure 3.15 (a) and (b) cyclic voltagrams of P3 and 2-b (3 mM) using 0.1M TBAPF <sub>6</sub> supporting
electrolyte at a scan rate of 0.1Vs <sup>-1</sup> in CHCl <sub>3</sub> , respectively. For clarity in Figure (a) both the oxidation
and reduction voltagrams were separated
Figure 3.16 (a) and (b) PM3 optimized chemical structures of monomer 2-b and complex 2-b-TFA,
respectively. Selected H-bonded lengths [Å] for <b>2-b</b> : N4N3-H= 3.42Å; N4N2-H= 2.88 Å; N1
N2-H= 2.52 Å; N1N3-H= 2.65 Å; for complex <b>2-b-TFA</b> : N1-HO1= 1.67 Å; N2-HO2=
2.56Å; N3-HO2= 2.77 Å

Figure 3.17(a) and (b) PM3 optimized chemical structures of monomer 2-b and complex 2-b-TFA,
and the molecular orbital distribution plots of their HOMO and LUMO states, respectively in the
ground state
Figure 3.18 TD-DFT optimized stable chemical structures of monomer A1. Molecular orbital
distribution plots of the HOMO and LUMO states, respectively, in the ground state and their
corresponding HOMO-1 and LUMO+1 plots in the excited state
Figure 3.19 TD-DFT optimized stable chemical structures of monomer D1. Molecular orbital
distribution plots of the HOMO and LUMO states, respectively, in the ground state and their
corresponding HOMO-1 and LUMO+1 plots in the excited state
Figure 3.20 TD-DFT optimized stable chemical structures of monomer D2 modeled for the polymer
in this study. Molecular orbital distribution plots of HOMO and LUMO states in the ground state and
their corresponding HOMO-1 and LUMO+1 plots in the excited state
Figure 3.21 DFT optimized stable chemical structures of monomer D2 modeled for the polymer in
this study and its side and top views, respectively. Dihedral angles between DPP and AKF ( $\Phi$ =
24.3°) along with main chain triazole units ( $\Phi = 56.5$ °) are presented in the top view picture of
<b>D2</b> 118
Figure 3.22 Thermogravimetric (TGA) analyses of polymers P3, P1, P2, and P4. 5% weight loss
temperature $(T_{d5})$ of each polymer was denoted
Figure 3.23 Powder XRD patterns of polymers P4 and P3.
Figure 3.24 (a) and (c) AFM-images of polymers P2 and P3, respectively. (b) and (d) rendered
AFM-3D images of (a) and (b). Scale bar (a) and (b) = 2 $\mu$ m; z-scale (a) = 6.2 nm and (c) = 2.5
nm 122

Figure 3.25 (a) and (b) AFM cross-sectional analysis of polymers P2 and P3. Marked
region analyses clearly denoting noticeable changes in their average height from 4.2 nm of <b>P2</b> to 1.5
nm of P3 confirmed the preserved interlocking nature as well as twisted geometry in MIPA. (scale
bar = 2 $\mu$ m; z-scale (a) = 6.2 nm and (b) = 2.5 nm)
Figure 3.26 Polymer P4. (a) AFM-image,(b) Rendered AFM-3D image, and (c) AFM cross-
sectional analysis. The average height of P4 was about 35 nm, however the average height of P3 was
about 1.5 nm, this distinctive low height of P3 was plausibly arose from its twisted geometry in
compare to <b>P4</b> with strong $\pi$ - $\pi$ interactions. (Scale bar = 2 $\mu$ m; z-scale (a) = 50.2
nm)
Figure 3.27 AFM image based depth analyses polymer P3, P2, and P4. Variation in the structural
and molecular dimension lengths in these MIPAs denoted that orthogonal H-bonded polymer P3
could be oriented in folded fashion
Figure 3.28 FE-SEM images of polymer P3 (a) in free state and (b) in protonated state with the
addition of TFA (1 M, 10 equiv in THF). Insets: the corresponding enlarged portions of (a) and (b),
respectively. (scale bar (a) = 10 $\mu$ m and (b) = 1 $\mu$ m, insets: scale bar (a) = 1 $\mu$ m and (b) = 100
nm)
Figure 3.29 FE-SEM images of polymer P3. (a) in free state (b) in the protonated state with the
addition of TFA (1 M, 10 equiv), and (c) in the recovered state by neutralization with DBU. Inset in
(c) magnified portion of spherical vesicle. (scale bar (a), (b) = 1 $\mu$ m, and (c) = 100 nm; inset of (c) =
100 nm)
Figure 3.30 TEM images of polymer P3 (a) in free state and (b) in protonated state with the addition
of TFA (1 M, 10 equiv in THF). Insets: the corresponding enlarged portions of (a) and (b),

respectively. (scale bar (a) and (b) = $500$ nm, insets: scale bar (a) = $200$ nm and (b) = $100$
nm)
Figure 3.31 (a) TEM image of polymer P3 in free form and estimated size of vesicle type particles
during its nano self-assembly process. (b) TEM image of P3 upon the addition of TFA and its
transformation in to hierarchical nano hexagonal sheets and estimated sizes of an individual
hexagonal sheet. (Scale bar (a) = $200 \text{ nm}$ and (b) = $50 \text{ nm}$ )
Figure 3.32 Variation in the hydrodynamic diameter of the polymer P3. (100 $\mu$ M solution in THF)
(a) P3 without TFA. (b) P3 with the addition of TFA (1 M, 10 equiv). (c) Recovered sample by
neutralization with DBU
Figure 3.33 Graphical representation of plausible hierarchical nano-self-assembly process of MIPAs
into bilayer vesicles and its acid driven transformation into hexagonal nano-sheets and fibers in a
reversible fashion. For legibility of the self-assembly process we denoted simple repeating monomer
unit of supramolecular polymer <b>P3</b> 131
Figure 4.1 Hydrazine triggered phthalimide deprotection with a fluorescent ratiometric response of
phthalimide appended hydroxyl 4-naphthalimide derivative
Figure 4.2 UV-vis absorption spectra change of probe $HZ$ (5 $\mu M$ ) upon addition of the hydrazine
(20 μM) in a mixture of PBS buffer (PBS, pH 7.2, 10 mM) and EtOH (1:9, v/v) solution, Inset
pictures depicting perceivable naked eye color change of probe <b>HZ</b> upon hydrazine addition140
Figure 4.3 Fluorescence spectra change of probe HZ (5 $\mu$ M) upon addition of the hydrazine (20 $\mu$ M)
in a mixture of PBS buffer (PBS, pH 7.2, 10 mM) and EtOH (1:9, v/v) solution, Inset pictures
depicting perceivable fluorescence color change (under UV lamp $\lambda = 365$ nm) of probe <b>HZ</b> upon
hydrazine addition $\lambda = 405 \text{ nm Slite: } 5 \text{ nm/ } 5 \text{ nm}$

<b>Figure 4.4</b> (a) Fluorescence responses of probe <b>HZ</b> (5 $\mu$ M) with various primary amines (25 $\mu$ M) in
a mixture of PBS buffer (PBS, pH 7.2, 10 mM) and EtOH (1:9, v/v) solution. Bars represent the
fluorescence intensity ratio in the presence and absence of various amines. Black bar represent the
addition of primary amines (25 $\mu$ M) to probe <b>HZ</b> (5 $\mu$ M). Red bars represent the subsequent addition
of hydrazine (25 $\mu$ M) to the solution. $0 = \text{hydrazine}$ , $1 = \text{hydroxyl}$ amine, $2 = \text{urea}$ , $3 = \text{thiourea}$ , $4 = \text{thiourea}$
monomethylamine, $5$ = ethylenediamine, $6$ = 1,4-Diaminobutane, $7$ = trans-1,2-Diaminocyclohexane,
8 = aqueous ammonia, and 9 = guanidine nitrate, respectively. (b) and (c) UV-vis and fluorescence
color changes under (UV lamp 365 nm) of probe HZ (5 $\mu$ M) with various amines (25 $\mu$ M)
sequentially from left to right hydroxyl amine, urea, thiourea, monomethylamine, ethylenediamine,
hydrazine, 1,4-Diaminobutane, trans-1,2-Diaminocyclohexane, aqueous ammonia, and guanidine
nitrate. $\lambda_{ex} = 405$ nm, Slits: 5 nm/ 5 nm
Figure 4.5 (a) Fluorescence spectra of probe HZ in the presence of hydrazine and other
representative primary amines. [HZ] = (5 $\mu$ M), [hydrazine], and [primary amines] = (25 $\mu$ M) in a
mixture of PBS buffer solutions (pH 7.2, 10 mM) and EtOH (1:9, v/v); (b) Fluorescence spectra of
Probe <b>HZ</b> (5 $\mu$ M) upon the (5 $\mu$ M) upon the titration of hydrazine (0-20 $\mu$ M)
Figure 4.6 (a) UV-vis absorption spectra of probe HZ (5 μM) upon titration with hydrazine (0-20
$\mu M$ ) in a mixture of PBS buffer solution (pH 7.2, 10 mM) in EtOH (1:9, $v/v$ ). (b) Ratiometric
calibration curve $A_{439 \text{ nm}}/A_{344 \text{ nm}}$
<b>Figure 4.7</b> (a) Fluorescent Ratiometric calibration curve $I_{528 \text{ nm}}/I_{467 \text{ nm}}$ ; (b) plot o fluorescent ratio
intensity change at two characteristic wavelengths 467 and 528 nm for the mixture of probe <b>HZ</b> (5
$\mu M)$ and hydrazine in a mixture of PBS buffer solution (pH 7.2, 10 mM) in EtOH (1:9, v/v) in the
range of $(0.7.5 \text{ µM}) \lambda = 405 \text{ nm}$ Slits: 5 nm/5 nm

Figure 4.8 (a) and (b) Semi-empirical PM3 method optimized HOMO and LUMO frontier molecular
orbital distributions of probe HZ, respectively (c) energy-minimized geometry of probe HZ.
Dihedral angle between phthalimide and naphthalimide plane was denoted which effectively blocked
the ICT-process. Mulliken charges of phthalimide and naphthalimide carbonyl carbons were denoted
in picture (c). Color coding of atoms blue = N, red = O, grey = C and white = H,
respectively
Figure 4.9 (a) and (b) Semi-empirical PM3 method optimized HOMO and LUMO frontier molecular
orbital distributions of compound HZA, respectively; (c) energy-minimized geometry of compound
HZA. Hydrazinolysis released the free amine and eventually enabling the ICT process. Color coding
of atoms blue = N, red = O, grey = C and white = H, respectively
Figure 4.10 <sup>1</sup> H NMR ( $d_6$ -DMSO, 300 MHz, 25 °C) stock plot. (a) Compound HZA (3 mM), (b)
probe HZ (3 mM) with the addition of hydrazine (2.0 equiv), and (c) probe HZ (3
mM)
<b>Figure 4.11</b> The mechanism for hydrazine selective phthalimide deprotection of probe <b>HZ</b> 147
Figure 4.12 (a) Fluorescent spectral changes if probe HZ (6 $\mu$ M) upon addition of hydrazine (30
$\mu M$ ) in a mixture of PBS buffer (PBS, pH 7.2, 10 mM) and EtOH (1:9, v/v) solution. The
fluorescent intensity data were collected after certain time intervals as depicted in the figure (a). (b)
Corresponding time dependent fluorescence ratio ( $I_{528}/I_{467}$ nm) and two characteristic wavelength
changes of probe <b>HZ</b> ; $\lambda_{ex} = 405$ nm, Slits: 5 nm/ 5 nm.
Figure 4.13 (a) Fluorescence spectra of probe HZ in the presence of hydrazine and other
representative metal ions. [HZ] = (5 $\mu$ M), [hydrazine] = (25 $\mu$ M), and [metal ions]= (50 $\mu$ M) in a
mixture of PBS buffer (pH 7.2, 10 mM) and EtOH (1:9), $v/v$ ). $\lambda_{ex} = 405$ nm, Slit: 5 nm/ 5 nm. (b)
Fluorescence responses of probe HZ (5 $\mu$ M) with various metal ions (50 $\mu$ M) in a mixture of PBS

buffer (pH 7.2, 10 mM) and EtOH (1:9, v/v) solution. Bars represent the fluorescence intensity ratio
in the presence and absence of various metal ions (Na <sup>+</sup> , Ag <sup>+</sup> , Ca <sup>2+</sup> , Zn <sup>2+</sup> , Cu <sup>2+</sup> , Ni <sup>2+</sup> , Cd <sup>2+</sup> , Hg <sup>2+</sup> ,
Pb <sup>2+</sup> , Ag <sup>2+</sup> , Fe <sup>3+</sup> and Al <sup>3+</sup> ). Black bar represent the addition of metal ions (50 $\mu$ M) to probe <b>HZ</b> (5
$\mu M$ ). Red bars represent the subsequent addition of hydrazine (25 $\mu M$ ) to the solution149
Figure 4.14 (a) Fluorescence spectra of probe HZ in the presence of hydrazine and other
representative anions. [HZ] = (5 $\mu$ M), [hydrazine] = (25 $\mu$ M), and [anions] = (50 $\mu$ M) in a mixture of
PBS buffer (pH 7.2, 10 mM) and EtOH (1:9), $v/v$ ). $\lambda_{ex} = 405$ nm, Slit: 5 nm/ 5 nm. (b) Fluorescence
responses of probe <b>HZ</b> (5 μM) with various anions (50 μM) in a mixture of PBS buffer (pH 7.2, 10
mM) and EtOH (1:9, v/v) solution. Bars represent the fluorescence intensity ratio in the presence and
absence of various anions (F, C1, Br, $\Gamma$ , AcO, NO <sub>3</sub> , H <sub>2</sub> PO <sub>4</sub> , N <sub>3</sub> , HCO <sub>3</sub> , ClO <sub>4</sub> SO <sub>4</sub> <sup>2</sup> and S <sub>2</sub> O <sub>8</sub> <sup>2</sup> ).
Black bar represent the addition of anions (50 $\mu$ M) to probe HZ (5 $\mu$ M). Red bars represent the
subsequent addition of hydrazine (25 μM) to the solution
Figure 4.15 (a) and (b) Fluorescence intensity changes of probe HZ (6 μM) and fluorescence
intensity changes of probe HZ (6 $\mu$ M) in the presence of hydrazine (12 $\mu$ M) as a function of pH in a
mixture of PBS buffer (pH 7.2, 10 mM) and EtOH (1:9), $v/v$ ), respectively. $\lambda ex = 405$ nm, Slits: 5
nm/5 nm
Figure 4. 16 <sup>1</sup> H NMR ( $d_6$ -DMSO, 300 MHz, 25 °C) stock plot. (a) Compound HZA (3 mM), (b)
probe $HZ$ (3 mM) with the addition of hydroxide in $D_2O$ (5.0 equiv), and (c) probe $HZ$ (3
mM)
<b>Figure 4. 17</b> ESI (+)-MS chromatogram of Probe <b>HZ</b> in acidic pH = 1.0 solution
<b>Figure 4.18</b> ESI (+)-MS chromatogram of Probe <b>HZ</b> in basic pH = 14.0 solution
Figure 4.19 (a), (b), (c) and (d) naked eye color changes of probe HZ free (5 μM), in the presence of
hydrazine (25 $\mu$ M), in the presence acidic solution (pH = 1.0), in the presence basic solution (pH =

14.0), respectively. (e)-(h) fluorescence color changes under UV lamp 365 nm of t	the respective (a)-
(d) solutions	153
Figure 4. 20 Fluorescence images of Hep G2 cells incubated with 10 $\mu M$ probe F	IZ for 15 min (b)
and then further incubated with 25 $\mu M$ hydrazine for 15 min (d). (a), (c) Bright-	field transmission
image of Hep G2 cells in (b) and (d). $\lambda_{ex} = 405 \text{ nm}$ .	155

